Kinetic and Related Models
©American Institute of Mathematical Sciences
Volume **4**, Number **1**, March **2011**
doi:10.3934/krm.2011.4.295
pp. **295–316**

COMPUTATIONAL HIGH FREQUENCY WAVE DIFFRACTION BY A CORNER VIA THE LIOUVILLE EQUATION AND GEOMETRIC THEORY OF DIFFRACTION

Shi Jin

Department of Mathematics, University of Wisconsin
Madison, WI 53706, USA

Dongsheng Yin

Department of Mathematical Sciences, Tsinghua University
Beijing, 100084, China

Dedicated to the memory of Carlo Cercignani

Abstract. We construct a numerical scheme based on the Liouville equation of geometric optics coupled with the Geometric Theory of Diffraction (GTD) to simulate the high frequency linear waves diffracted by a corner. While the reflection boundary conditions are used at the boundary, a diffraction condition, based on the GTD theory, is introduced at the vertex. These conditions are built into the numerical flux for the discretization of the geometrical optics Liouville equation. Numerical experiments are used to verify the validity and accuracy of this new Eulerian numerical method which is able to capture the physical observable of high frequency and diffracted waves without fully resolving the high frequency numerically.

1. **Introduction.** In this paper, we construct a numerical scheme based on the Liouville equation to approximate the high frequency wave equation in two-dimension:

$$u_{tt} - c(\mathbf{x})^2 \Delta u = 0, \ t > 0, \tag{1.1}$$

$$u(0) = A(\mathbf{x}, 0) e^{i\phi(\mathbf{x},0)/\epsilon}, \tag{1.2}$$

$$\frac{\partial u}{\partial t}(0) = B(\mathbf{x}, 0) e^{i\phi(\mathbf{x},0)/\epsilon}, \tag{1.3}$$

here $c(\mathbf{x})$ is the local wave speed and $\epsilon \ll 1$. When the *essential frequencies* in the wave field are relatively high, and thus the wavelength is short compared to the size of the computational domain, direct simulation of the standard wave equation will be very costly, and approximate models for wave propagation based on geometric optics (GO) are usually used [10, 13].

2000 *Mathematics Subject Classification.* Primary: 65M06, 78A45, 35L05; Secondary: 65Z05, 34E05.

Key words and phrases. Geometrical Theory of Diffraction, Liouville equation, High frequency wave.

The first author is supported by NSF grant No. DMS-0608720, NSF FRG grant DMS-0757285, a Van Vleck Distinguished Research Prize and a Vilas Associate Award from the University of Wisconsin-Madison, and the second author is supported by NSFC grant No. 10901091 and NSFC grant No. 10826027.

We are concerned with the case when there are some wedges in the computational domain, which contain tips (vertices) and boundaries. When waves hit the vertices, there will be diffractions in all directions.

One of the approximate models for high frequency wave equation is the Liouville equation, which arises in phase space description of geometric optics (GO) [10, 35]:

$$f_t + H_{\mathbf{v}} \cdot \nabla_{\mathbf{x}} f - H_{\mathbf{x}} \cdot \nabla_{\mathbf{v}} f = 0, \ t > 0, \ \mathbf{x}, \mathbf{v} \in R^d, \tag{1.4}$$

where the Hamiltonian H possesses the form

$$H(\mathbf{x}, \mathbf{v}) = c(\mathbf{x})|\mathbf{v}| = c(\mathbf{x})\sqrt{v_1^2 + v_2^2 + \cdots + v_d^2}, \tag{1.5}$$

$f(t, \mathbf{x}, \mathbf{v})$ is the energy density distribution of particles depending on position $\mathbf{x}$, time t and slowness vector $\mathbf{v}$.

The bicharacteristics of this Liouville equation (1.4) satisfies the Hamiltonian system:

$$\frac{d\mathbf{x}}{dt} = c(\mathbf{x})\frac{\mathbf{v}}{|\mathbf{v}|}, \quad \frac{d\mathbf{v}}{dt} = -c_{\mathbf{x}}|\mathbf{v}|. \tag{1.6}$$

The derivation of GO does not take into account the effects of geometry of the domain and boundary conditions, which lead to discontinuous GO solutions in some regions. Diffractions are lost in the infinite frequency approximation such as the Liouville equation. In this case, correction terms can be derived, as done in the *Geometric Theory of Diffraction* (GTD) by Keller in [26]. The GTD provides a systematic technique for adding diffraction effects to the GO approximations.

The methods for computing the GO solutions can be divided into Lagrangian and Eulerian methods.

Lagrangian methods are based on the ODEs (1.6). The simplest Lagrangian method is the ray tracing method where the ODEs in (1.6) together with ODEs for the amplitude are solved directly with numerical methods for ODEs. This approach is very popular in standard free space GO, [5], and the diffractions, [2, 9]. The ray tracing method gives the phase and amplitude of a wave along a ray tube, and interpolation must be applied to obtain those quantities everywhere when rays diverge. Such interpolations can be very complicated for diverging rays. On the other hand, in the ray tracing method, when a ray hits the vertex of the corner, it will produce diffraction rays in all directions. *In computations, one incident ray must be divided into many diffraction rays to simulate the diffractions, which adds the computational cost dramatically.*

In the last decade, Eulerian methods based on PDEs have been proposed to avoid some of the drawbacks of the ray tracing method [1]. Eulerian methods discretize the PDEs on fixed computational grids to control errors everywhere and there is no need for interpolation. The simplest Eulerian method solves the eikonal and transport equations in GO. This technique has been used in standard GO [13]. However, the eikonal and transport equations pick up the so-called viscosity solution [8], which are not adequate beyond caustics. Rather, the solutions become multivalued, and more elaborate schemes must be devised. Recently several phase space based level set methods for high frequency waves, in particular the multivalued solutions in GO are based on the Liouville equations, see [6, 11, 14, 18, 19, 33].

More recently, a class of Hamiltonian-preserving numerical schemes for the Liouville equation (1.4) were developed to take into account partial transmissions and reflections [17, 20, 21, 22] for high frequency waves through interfaces.

There are very few results on Eulerian methods for diffractions. In this direction, we mention recent numerical methods for creeping waves [31, 32, 42]. For curved interfaces, the authors [24] constructed an Eulerian method for diffraction at interfaces that takes into consideration of partial transmissions, reflections and diffractions. The idea was to revise the transmission/reflection interface condition used by Jin and Wen [20, 21] for the Liouville equation in the case of critical and tangent angles to account for diffractions. The diffraction coefficients and decay rates derived in GTD are used in the interface condition. These interface conditions are then built into the numerical fluxes for the Liouville solver. Such an Eulerian computational method is able to capture the moments of high frequency waves without–at least away from the interfaces–numerically resolving the high frequencies, yet still captures the correct interface scattering and diffractions. In [25], we also derived such a numerical scheme for high frequency wave diffraction by a half plane.

This paper is to further our previous work [25] to a different geometry, namely, waves through a corner. When a wave hits a corner, it usually reflects. However, at the vertex of the corner, it generates diffracted waves into *all* directions. In particular, the diffracted waves can reach the shadow zone–the zone that the GO theory cannot cover. We provide a diffraction condition, based on the GTD theory, at the vertex to reflect this diffraction nature. We then build this condition, as well as the reflection boundary condition, into the numerical flux of the Liouville solver, in order to capture the diffractions.

This paper is organized as follows. The GO approximations by the Wigner transform for wave equation are sketched in Section 2. In Section 3, we present the behavior of waves at a corner based on the GTD theory, and provide the conditions for (1.4) that account for reflections at the boundary of the corner and diffractions at the vertex of the corner. In Section 4, the diffraction conditions derived in the previous section is built into the numerical flux in the two space dimension. In section 5, we study the positivity and l^∞ stability of the numerical scheme. Numerical examples are given in section 6 to validate the model and to verify the accuracy of the scheme against the full simulation based on the original wave equation (1.1)-(1.3). Finally, we make some concluding remarks.

2. Geometric optics approximation of the wave equation in phase space.

Consider the two dimensional wave equation

$$u_{tt} - c(\mathbf{x})^2 \Delta u = 0, \qquad \mathbf{x} \in R^2,\ t \in R, \tag{2.1}$$

$$u\big|_{t=0} = u_I, \quad u_t\big|_{t=0} = s_I. \tag{2.2}$$

We introduce the new dependent variables

$$s = u_t, \quad \mathbf{r} = \nabla u,$$

to obtain the system

$$\begin{cases} \dfrac{\partial \mathbf{r}}{\partial t} - \nabla s = 0, \\ \dfrac{1}{c(\mathbf{x})^2}\dfrac{\partial s}{\partial t} - \mathrm{div}\mathbf{r} = 0. \end{cases} \tag{2.3}$$

The energy density is given by

$$\mathcal{E}(\mathbf{x}, t) = \frac{1}{2}\frac{1}{c(\mathbf{x})^2}|u_t|^2 + \frac{1}{2}|\nabla u|^2. \tag{2.4}$$

Let $\mathbf{w} = (\frac{\partial u}{\partial x_1}, \frac{\partial u}{\partial x_2}, s)$, system (2.3) can be put in the form of a symmetric hyperbolic system

$$A(\mathbf{x})\frac{\partial \mathbf{w}}{\partial t} + \sum_i D_i \frac{\partial \mathbf{w}}{\partial x_i} = 0, \tag{2.5}$$

with initial data

$$\mathbf{w}(0, \mathbf{x}) = \mathbf{w}_0(\mathbf{x}).$$

The matrix $A(\mathbf{x}) = \mathrm{diag}(1, 1, \frac{1}{c(\mathbf{x})^2})$, while each of the matrices D_i is constant and symmetric with entries either 0 or -1.

To study the GO limit of solution of (2.5), we assume that the coefficients of the matrix $A(\mathbf{x})$ vary on a scale much longer than the scale on which the initial data vary. Let ϵ be the ratio of these two scales. Rescaling space and time coordinates $(\mathbf{x}, t)$ by $\mathbf{x} \to \epsilon\mathbf{x}, t \to \epsilon t$, one obtains

$$A(\mathbf{x})\frac{\partial \mathbf{w}^\epsilon}{\partial t} + \sum_i D_i \frac{\partial \mathbf{w}^\epsilon}{\partial x_i} = 0, \tag{2.6}$$

$$\mathbf{w}^\epsilon(0, \mathbf{x}) = \mathbf{w}_0(\frac{\mathbf{x}}{\epsilon}) \quad \text{or} \quad \mathbf{u}_0(\frac{\mathbf{x}}{\epsilon}, \mathbf{x}). \tag{2.7}$$

Note that the parameter ϵ does not appear explicitly in (2.6). It enters through the initial data (2.7). We are interested in the initial data of the standard WKB form

$$\mathbf{w}^\epsilon(0, \mathbf{x}) = A_0(\mathbf{x})e^{iS_0(x)/\epsilon}. \tag{2.8}$$

Following [34], one can study the GO limit of (2.6) by using the Wigner distribution matrix W^ϵ:

$$W^\epsilon(t, \mathbf{x}, \mathbf{k}) = \Big(\frac{1}{2\pi}\Big)^n \int e^{i\mathbf{k}\cdot\mathbf{y}} \mathbf{w}^\epsilon(t, \mathbf{x} - \epsilon\mathbf{y}/2)\overline{\mathbf{w}^\epsilon(\mathbf{x} + \epsilon\mathbf{y}/2)}^t d\mathbf{y}, \tag{2.9}$$

where n is the space dimension and $\overline{\mathbf{w}}^t$ is the conjugate transpose of $\mathbf{w}$. Although W^ϵ is not positive definite, it becomes so as $\epsilon \to 0$.

The energy density for (2.6) is given by

$$\mathcal{E}^\epsilon(t, \mathbf{x}) = \frac{1}{2}(A(\mathbf{x})\mathbf{w}^\epsilon(t, \mathbf{x}), \mathbf{w}^\epsilon(t, \mathbf{x})) = \frac{1}{2}\int \mathrm{Tr}(A(\mathbf{x})W^\epsilon(t, \mathbf{x}, \mathbf{k}))d\mathbf{k}. \tag{2.10}$$

Let

$$\lim_{\epsilon\to 0} W^\epsilon(t, \mathbf{x}, \mathbf{k}) = W^{(0)}(t, \mathbf{x}, \mathbf{k}).$$

As $\epsilon \to 0$, the high frequency limit of $\mathcal{E}^\epsilon(t, \mathbf{x})$ is

$$\mathcal{E}^{(0)}(t, \mathbf{x}) = \frac{1}{2}\int \mathrm{Tr}(A(\mathbf{x})W^{(0)}(t, \mathbf{x}, \mathbf{k}))d\mathbf{k} = \int a^+(t, \mathbf{x}, \mathbf{k})d\mathbf{k}, \tag{2.11}$$

where the amplitude $a^\pm(t, \mathbf{x}, \mathbf{k})$ is given by

$$a^\pm(t, \mathbf{x}, \mathbf{k}) = \frac{1}{(2\pi)^2}\int d\mathbf{y}e^{i\mathbf{k}\cdot\mathbf{y}} f_\pm(t, \mathbf{x}, \mathbf{x} - \mathbf{y}/2, \mathbf{k})\overline{f_\pm(t, \mathbf{x}, \mathbf{x} + \mathbf{y}/2, \mathbf{k})}, \tag{2.12}$$

with

$$f_\pm(t, \mathbf{x}, \mathbf{z}, \mathbf{k}) = \sqrt{\frac{1}{2}}(\nabla u(t, \mathbf{z}) \cdot \hat{\mathbf{k}}) \pm \frac{\sqrt{2}}{2|c(\mathbf{x})|}\frac{\partial u}{\partial t}(t, \mathbf{z}), \tag{2.13}$$

and $\hat{\mathbf{k}} = (\cos\theta, \sin\theta)^t$. This shows that

$$a^+(t, \mathbf{x}, \mathbf{k}) = a^-(t, \mathbf{x}, -\mathbf{k}), \tag{2.14}$$

and therefore one needs only to keep track of $a^+(t, \mathbf{x}, \mathbf{k})$. It satisfies the Liouville equation [34]

$$\frac{\partial a^+}{\partial t} + c(\mathbf{x})\hat{\mathbf{k}} \cdot \nabla_{\mathbf{x}} a^+ - |\mathbf{k}| \nabla_{\mathbf{x}} c(\mathbf{x}) \cdot \nabla_{\mathbf{k}} a^+ = 0. \tag{2.15}$$

Therefore, a^+ can be interpreted as phase space energy density distribution. It solves the Liouville equations (1.4)-(1.5), with the zeroth moment giving the spatial energy density $\mathcal{E}^{(0)}(t, \mathbf{x})$ as in (2.11).

The GO approximation is good when ϵ is very small. For moderately small ϵ, diffraction can not be ignored in many applications. Clearly, the Liouville equation (2.15), valid at $\epsilon = 0$, does not contain any information about reflection, which occurs even for $\epsilon = 0$, nor diffraction which occurs for $\epsilon > 0$. It is not valid near the vertex of the wedge. In the next section, we will discuss the behavior at a corner.

3. **Wave behavior at a corner.** In GO, a wave moves with its energy distribution governed by the Liouville equation (1.4). When an incident wave hits the edge of a wedge, it will be completely reflected back [30]. According to the GTD, when the wave hits the vertex of the wedge, it will produce diffracted waves into all directions (see Fig. 1),

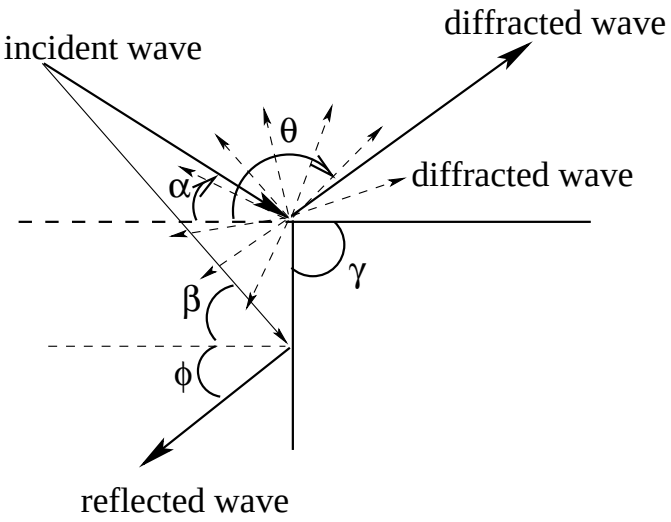

FIGURE 1. Diffraction by corner

The diffraction coefficients D_o is given by Keller [27] as

$$D_o(\theta, \alpha) = \frac{\epsilon \sin^2 \frac{\pi}{q}}{2q^2 \pi r} \left[\frac{1}{\cos \frac{\pi}{q} - \cos \frac{\theta - \alpha}{q}} \mp \frac{1}{\cos \frac{\pi}{q} - \cos \frac{\theta + \alpha + \pi}{q}} \right]^2,$$

with $\gamma = (2-q)\pi$, α is the incident angle, θ is the diffracted angle, both of which are defined in $(-\pi/2, \pi)$. The upper sign applies when the boundary condition on the edge of the wedge is $u = 0$ (soft boundary condition), while the lower sign applies if it is $\frac{\partial u}{\partial n} = 0$ (hard boundary condition) on the edge of the wedge.

A half plane is the case for $q = 2$, for which D_o is given by

$$D_o^{\pm}(\theta, \alpha) = \frac{\epsilon}{8\pi r} [\sec \frac{1}{2}(\theta - \alpha) \pm \csc \frac{1}{2}(\theta + \alpha)]^2.$$

In this paper, we only consider the case of a corner ($\gamma = \pi/2, q = 3/2$). In this case, the diffraction coefficient is

$$D_0^{\pm}(\theta,\alpha) = \frac{2\epsilon}{9\pi r}\Big[\frac{1}{\cos\frac{2}{3}\pi - \cos\frac{2}{3}(\theta-\alpha)} \mp \frac{1}{\cos\frac{2}{3}\pi - \cos\frac{2}{3}(\theta+\alpha+\pi)}\Big]. \tag{3.16}$$

In the GTD, the considered wave propagation phenomena are the incident direct illumination, reflection, and diffraction by vertex of the corner.

If $-\frac{1}{2}\pi < \alpha < 0$, the above diffraction coefficient is not valid when $\theta = \pi + \alpha$ or $\theta = -\alpha$ i.e. near the shadow boundary and the reflection boundary, and if $\frac{1}{2}\pi < \alpha < \pi$, the diffraction coefficient is not correct when $\theta + \alpha = \pi$ (the reflection boundary) or $\alpha - \theta = \pi$ (the shadow boundary). There are boundary layer near the shadow boundary and the reflection boundary, with thickness of order $\epsilon^{1/2}$. When $0 < \alpha < \frac{1}{2}\pi$, there are no shadow boundary and reflection boundary, the diffraction coefficient (3.16) is correct.

The *Uniform Geometric Theory of Diffraction* (UTD) [28] can overcome this difficulty by introducing the transition functions. The uniform diffraction coefficient for UTD is given by

$$\begin{aligned} D(\theta,\alpha)^{\pm} =& \frac{2\epsilon}{9\pi r}\Big|\cot\Big(\frac{\pi+(\theta-\alpha)}{3}\Big)F[\epsilon^{-1}ra^{+}(\theta-\alpha)] \\ &+ \cot\Big(\frac{\pi-(\theta-\alpha)}{3}\Big)F[\epsilon^{-1}ra^{-}(\theta-\alpha)] \\ &\mp\Big\{\cot\Big(\frac{\pi+(\theta+\alpha)}{3}\Big)F[\epsilon^{-1}ra^{+}(\theta+\alpha)] \\ &+ \cot\Big(\frac{\pi-(\theta+\alpha)}{3}\Big)F[\epsilon^{-1}ra^{-}(\theta+\alpha)]\Big\}\Big|^2, \end{aligned} \tag{3.17}$$

where the transition function

$$F(X) = 2i\sqrt{X}\exp(iX)\int_{\sqrt{X}}^{\infty}\exp(-i\tau^2)d\tau\,,$$

in which one takes the principle (positive) branch of the square root, and

$$\alpha^{\pm}(\beta) = 2\cos^2\Big(\frac{3N^{\pm}\pi - (\beta)}{2}\Big),$$

in which $N^{\pm}$ are the integers which most nearly satisfy the equations

$$\begin{aligned} 3\pi N^{+} - (\beta) &= \pi, \\ 3\pi N^{-} - (\beta) &= -\pi, \end{aligned}$$

with

$$(\beta) = \theta \pm \alpha.$$

$\alpha^{\pm}(\beta)$ is a measure of the angular separation between the field point and a shadow or reflection boundary.

The magnitude of the transition function $F(x)$ and the original diffraction coefficient D_o with incident angle $\alpha = -\frac{9}{20}\pi$ and diffraction angle $-\frac{1}{2}\pi \le \theta < \frac{9}{20}\pi$ are presented in Fig. 2. One can see that D_o goes to infinite when θ approaches $\frac{9}{20}\pi$, i.e. at the reflection boundary. On the other hand, the magnitude of $F(x)$ is very small when $x \ll 1$, and $|F(x)| \approx 1$ when $x \gg 1$. Then the discontinuity in the geometrical-optics field at the reflection boundary is compensated by the transition function, while outside of the transition regions these factors are approximately

one, and Keller's expressions for the diffraction coefficients D_o are obtained. The behavior near the shadow boundary is similar.

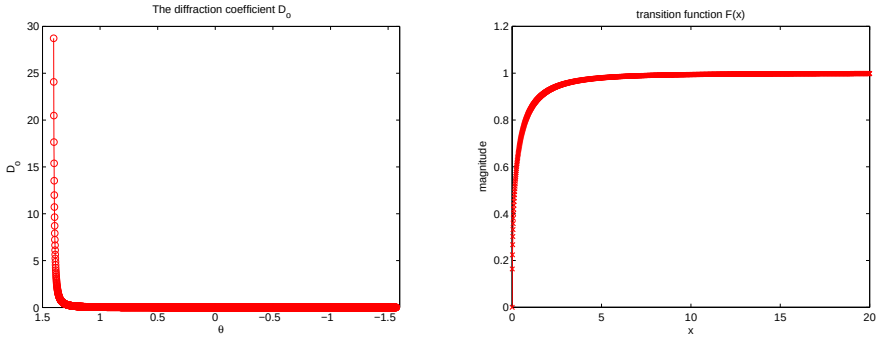

FIGURE 2. The diffraction coefficient D_o and the transition function $F(x)$

We will discuss the wave behavior at the corner in more details. Assume the boundary of the corner is $\Gamma_1 = \{(x,y) \mid x > x_0, y = y_0\}, \Gamma_2 = \{(x,y) \mid x = x_0, y < y_0\}$, and the vertex of the corner is (x_0, y_0). See Fig. (3) where (x_0, y_0) is marked as $(x_{i_0+1/2}, y_{j_0+1/2})$.

Let $\mathbf{x} = (x,y)$ and $\mathbf{v} = (\xi, \eta)$. Assume the incident wave hits the corner with velocity (ξ, η). There are two possibilities:

1. If the wave hits the corner at Γ_1, it will be completely reflected back with velocity $(\xi, -\eta)$. If the wave hits the corner at Γ_2, it will be completely reflected back with velocity $(-\xi, \eta)$.
2. The wave hits the vertex (x_0, y_0) of the corner. In this case, according to the GTD, the wave can partly diffract and partly travel in the original direction. Introduce the polar coordinates by
$$\xi = R\cos\alpha, \ \eta = R\sin\alpha, \quad R = \sqrt{\xi^2 + \eta^2}\,. \tag{3.18}$$
With the diffraction coefficient $D(\theta, \alpha)$, the wave is diffracted with new velocities $(\xi_d, \eta_d), d = 1, 2, \cdots$, with
$$\xi_d = R_d\cos\theta, \ \eta_d = R_d\sin\theta \ R_d = \sqrt{\xi_d^2 + \eta_d^2},$$
where $D(\theta, \alpha)$ is given by (3.17) if $-\frac{1}{2}\pi < \alpha < 0$ or $\frac{1}{2}\pi < \alpha < \pi$, and by (3.16) if $0 < \alpha < \frac{1}{2}\pi$.

The solution to the Liouville equation, which is linearly hyperbolic, can be solved by the method of characteristic. Namely, the density distribution f remains a constant along a bicharacteristics. However, we need to provide suitable conditions for the Liouville equation to account for boundary reflections and vertex diffractions. For the wave hitting the corner at Γ_1, it will be completely reflected with new velocity $(\xi, -\eta)$, and the following condition will be used
$$f(t, x, y_0, \xi, \eta) = f(t, x, y_0, \xi, -\eta). \tag{3.19}$$
If the wave hit the corner at Γ_2, it will be completely reflected with new velocity $(-\xi, \eta)$, and the following reflecting boundary condition will be used,
$$f(t, x_0, y, \xi, \eta) = f(t, x_0, y, -\xi, \eta). \tag{3.20}$$

At the vertex of the corner, we use the following diffraction condition:

1. if $-\frac{1}{2}\pi < \theta < 0$, or $\frac{1}{2}\pi < \theta < \pi$, then

$$f_+(t,x_0,y_0,R,\theta) = \int_{-\frac{\pi}{2}}^{\pi} D(\theta,\alpha) f_-(t,x_0,y_0,R,\alpha)d\alpha + \big(1 - \int_{-\frac{\pi}{2}}^{\pi} D(\theta,\alpha)d\alpha\big) f_-(t,x_0,y_0,R,\theta), \tag{3.21}$$

   with $f_\pm(t,\mathbf{x},\mathbf{v}) = \lim_{\sigma\to 0} f(t,\mathbf{x}\pm\sigma\mathbf{v},\mathbf{v}), R = \sqrt{\xi^2+\eta^2}$.
2. if $0 < \theta < \frac{1}{2}\pi$, then

$$f_+(t,x_0,y_0,R,\theta) = \int_{-\frac{\pi}{2}}^{\pi} D(\theta,\alpha) f_-(t,x_0,y_0,R,\alpha)d\alpha. \tag{3.22}$$

We will explain the conditions (3.21) and (3.22). When a wave hits the corner besides the vertex, it will be completely reflected with a negative momentum in each direction. But when a particle hits the vertex of the corner with an incident angle α, it will be diffracted at angle θ with diffraction coefficient $D(\theta,\alpha)$; and the energy of the particle $c(\mathbf{x})|\mathbf{v}| = c(\mathbf{x})\sqrt{\xi^2+\eta^2} = c(\mathbf{x})R$ will not change. In (3.21), the density distribution function of waves $f_+(t,x_0,y_0,\xi,\eta)$ is a superposition of the incident wave that passes through the vertex, and all diffracted waves, generated by other incident waves, that move in the direction of $\mathbf{v} = (\xi,\eta)$. In (3.21), there are only the diffracted waves generated from the vertex of corner in this region, since no incident wave in this direction is possible (since they would have to emerge from inside the wedge, which is impossible).

Note a condition on D in (3.21) is

$$\int_{-\pi/2}^{\pi} D(\theta,\alpha)\, d\alpha \le 1 \quad \text{for any}\theta\,.$$

These conditions will be used in the next section to construct the numerical flux on the corner.

4. **The numerical scheme.**

4.1. **The numerical flux.**

We use the Liouville equation

$$f_t + \frac{c(x,y)\xi}{\sqrt{\xi^2+\eta^2}} f_x + \frac{c(x,y)\eta}{\sqrt{\xi^2+\eta^2}} f_y - c_x\sqrt{\xi^2+\eta^2} f_\xi - c_y\sqrt{\xi^2+\eta^2} f_\eta = 0, \tag{4.1}$$

with boundary condition (3.19)-(3.22) to simulate high frequency wave equation (1.1).

Without loss of generality, we employ a uniform mesh with grid points at $x_{i+\frac{1}{2}}, i = 0,\cdots,M$ in the x direction, $y_{j+\frac{1}{2}}, j = 0,\cdots,N$ in the y direction, $\xi_{k+\frac{1}{2}}, k = 0,\cdots,K$ in the ξ direction and $\eta_{l+\frac{1}{2}}, l = 0,\cdots,L$ in the η direction. The cells are centered at (x_i,y_j,ξ_k,η_l) with $x_i = \frac{1}{2}(x_{i-\frac{1}{2}} + x_{i+\frac{1}{2}}), y_j = \frac{1}{2}(y_{j-\frac{1}{2}} + y_{j+\frac{1}{2}}), \xi_k = \frac{1}{2}(\xi_{k-\frac{1}{2}} + \xi_{k+\frac{1}{2}}), \eta_l = \frac{1}{2}(\eta_{l-\frac{1}{2}} + \eta_{l+\frac{1}{2}})$. The mesh sizes are denoted by $\Delta x = x_{i+\frac{1}{2}} - x_{i-\frac{1}{2}}, \Delta y = y_{j+\frac{1}{2}} - y_{j-\frac{1}{2}}, \Delta\xi = \xi_{k+\frac{1}{2}} - \xi_{k-\frac{1}{2}}, \Delta\eta = \eta_{l+\frac{1}{2}} - \eta_{l-\frac{1}{2}}$. Assume the vertex of the corner is $(x_{i_0+1/2}, y_{j_0+1/2})$, and the two boundary $\Gamma_1 = \big\{(x,y) \;\big|\; x > x_{i_0+\frac{1}{2}}, y = y_{j_0+\frac{1}{2}}\big\}, \Gamma_2 = \big\{(x,y) \;\big|\; x = x_{i_0+\frac{1}{2}}, y < y_{j_0+\frac{1}{2}}\big\}$ (see Fig. 3).

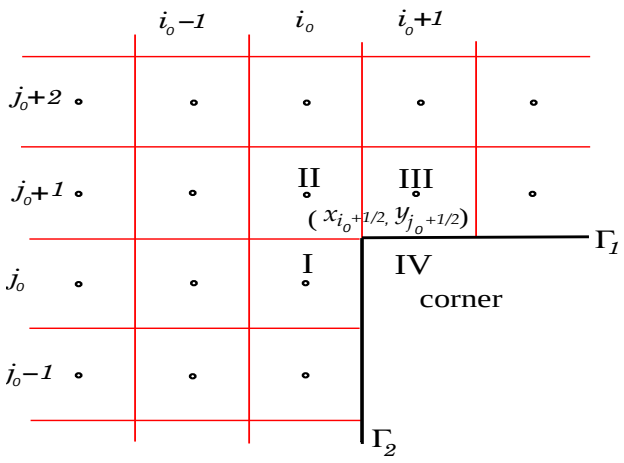

FIGURE 3. Meshes near the corner

Let Δt be the time step, $t^n = n\Delta t$. The cell average of f is defined as

$$f_{ijkl} = \frac{1}{\Delta x \Delta y \Delta \xi \Delta \eta} \int_{x_{i-\frac{1}{2}}}^{x_{i+\frac{1}{2}}} \int_{y_{j-\frac{1}{2}}}^{y_{j+\frac{1}{2}}} \int_{\xi_{k-\frac{1}{2}}}^{\xi_{k+\frac{1}{2}}} \int_{\eta_{l-\frac{1}{2}}}^{\eta_{l+\frac{1}{2}}} f(x,y,\xi,\eta) d\eta d\xi dy dx, \tag{4.2}$$

where $f^n_{ijkl} = f_{ijkl}(t^n)$. We approximate $c(x,y)$ by a piecewise bilinear function.

The 2D Liouville equation (4.1) can be discretized spatially as

$$\begin{aligned}(f_{ijkl})_t \quad &+ \quad \frac{c_{ij}\xi_k}{\Delta x\sqrt{\xi_k^2+\eta_l^2}}(f_{i+\frac{1}{2},jkl} - f_{i-\frac{1}{2},jkl}) + \frac{c_{ij}\eta_l}{\Delta y\sqrt{\xi_k^2+\eta_l^2}}(f_{i,j+\frac{1}{2},kl} - f_{i,j-\frac{1}{2},kl}) \\ &- \quad \frac{c_{i+\frac{1}{2},j} - c_{i-\frac{1}{2},j}}{\Delta x \Delta \xi}\sqrt{\xi_k^2+\eta_l^2}(f_{ij,k+\frac{1}{2},l} - f_{ij,k-\frac{1}{2},l}) \\ &- \quad \frac{c_{i,j+\frac{1}{2}} - c_{i,j-\frac{1}{2}}}{\Delta y \Delta \eta}\sqrt{\xi_k^2+\eta_l^2}(f_{ijk,l+\frac{1}{2}} - f_{ijk,l-\frac{1}{2}}) = 0.\end{aligned}$$

Here all the numerical fluxes are defined using the upwind discretization, except for $f_{i_0\pm\frac{1}{2},jkl}, j \le j_0+1, f_{i,j_0+1\pm\frac{1}{2},kl}, i \ge i_0$. We will use the conditions (3.19)– (3.21) to construct these fluxes.

Firstly, we divide the interval $[-\frac{1}{2}\pi, \pi]$ into 3I subinterval $[\alpha_m, \alpha_{m+1}], \alpha_m = m\Delta\alpha - \frac{1}{2}\pi, \Delta\alpha = \pi/2I, m = 0, 1, \cdots, 3I-1$. Let $R_{kl} = \sqrt{\xi_k^2+\eta_l^2}$ with

$$\xi_k = R_{kl}\cos\theta_{kl}, \quad \eta_l = R_{kl}\sin\theta_{kl}.$$

We first define f at $(x_{i_0+\frac{1}{2}}, y_{j_0+\frac{1}{2}})$. f at this point is affected by three neighboring cells surrounding the point $(x_{i_0+\frac{1}{2}}, y_{j_0+\frac{1}{2}})$. It is the summation of incoming and diffracted waves from these three cells.

1. If $\xi_k > 0, \eta_k > 0$, the incoming wave is from cell I, while the diffracted waves are from cells I, II & III.

$$\begin{aligned} f_{i_0+\frac{1}{2},j_0+\frac{1}{2},k,l} = & \Big[\sum_{m=0}^{I} D(\theta_{kl},\alpha_m) f_{i_0,j_0}(\xi_{klm},\eta_{klm}) \\ & + \sum_{m=I+1}^{2I} D(\theta_{kl},\alpha_m) f_{i_0,j_0+1}(\xi_{klm},\eta_{klm}) \\ & + \sum_{m=2I+1}^{3I} D(\theta_{kl},\alpha_m) f_{i_0+1,j_0+1}(\xi_{klm},\eta_{klm}) \Big] \Delta\alpha \\ & + \left[1 - \sum_{I=0}^{3I} D(\theta_{kl},\alpha_m)\Delta\alpha \right] f_{i_0,j_0}(\xi_k,\eta_l), \end{aligned} \tag{4.3}$$

with $\xi_{klm} = R_{kl}\cos\alpha_m, \eta_{klm} = R_{kl}\sin\alpha_m$. The first three terms in the right of the above equality represent the diffracted waves from I, II and III, respectively, while the last term is the incident wave hitting the corner with incident angle (ξ_k, η_l). Since (ξ_{klm}, η_{klm}) may not be grid points, we have to define them approximately. One can first locate the cell centers that bound these velocities, and then use a bilinear interpolation to evaluate the value at (ξ_{klm}, η_{klm}).

2. If $\xi_k < 0, \eta_l < 0$, the incoming wave is from cell III, while the diffracted waves are from cells I, II & III,

$$\begin{aligned} f_{i_0+\frac{1}{2},j_0+\frac{1}{2},k,l} = & \Big[\sum_{m=0}^{I} D(\theta_{kl},\alpha_m) f_{i_0,j_0}(\xi_{klm},\eta_{klm}) \\ & + \sum_{m=I+1}^{2I} D(\theta_{kl},\alpha_m) f_{i_0,j_0+1}(\xi_{klm},\eta_{klm}) \\ & + \sum_{m=2I+1}^{3I} D(\theta_{kl},\alpha_m) f_{i_0+1,j_0+1}(\xi_{klm},\eta_{klm}) \Big] \Delta\alpha \\ & + \left[1 - \sum_{I=0}^{3I} D(\theta_{kl},\alpha_m)\Delta\alpha \right] f_{i_0+1,j_0+1}(\xi_k,\eta_l). \end{aligned} \tag{4.4}$$

3. If $\xi_k > 0, \eta_l < 0$. This wave direction is moving toward cell IV. Since no diffracted wave will move in this direction. $f_{i_0+\frac{1}{2},j_0+\frac{1}{2},k,l}$ only comes from cell II,

$$f_{i_0+\frac{1}{2},j_0+\frac{1}{2},k,l} = f_{i_0,j_0+1}(\xi_k,\eta_l). \tag{4.5}$$

4. If $\xi_k < 0, \eta_l > 0$. The wave is moving toward cell II. Since no wave comes from cell IV, in this case, $f_{i_0+\frac{1}{2},j_0+\frac{1}{2},k,l}$ is only the sum of diffracted waves

from cells I, II and III.

$$
\begin{aligned}
f_{i_0+\frac{1}{2},j_0+\frac{1}{2},k,l} = \Big[& \sum_{m=0}^{I} D(\theta_{kl},\alpha_m) f_{i_0,j_0}(\xi_{klm},\eta_{klm}) \\
& + \sum_{m=I+1}^{2I} D(\theta_{kl},\alpha_m) f_{i_0,j_0+1}(\xi_{klm},\eta_{klm}) \\
& + \sum_{m=2I+1}^{3I} D(\theta_{kl},\alpha_m) f_{i_0+1,j_0+1}(\xi_{klm},\eta_{klm}) \Big] \Delta\alpha.
\end{aligned} \tag{4.6}
$$

Note $(x_{i_0+\frac{1}{2}}, y_{j_0+\frac{1}{2}})$ is not where we define the numerical flux. We now define the fluxes at $(x_{i_0}, y_{j_0+\frac{1}{2}})$ and $(x_{i_0+\frac{1}{2}}, y_{j_0+1})$ in an upwind way as follows,

- If $\xi_k < 0$, then

$$
f_{i_0,j_0+\frac{1}{2},k,l} = f_{i_0+\frac{1}{2},j_0+\frac{1}{2},k,l}, \ \forall l. \tag{4.7}
$$

- If $\eta_l > 0$, then

$$
f_{i_0+\frac{1}{2},j_0+1,k,l} = f_{i_0+\frac{1}{2},j_0+\frac{1}{2},k,l}, \ \forall k. \tag{4.8}
$$

For the numerical fluxes $f_{i_0+\frac{1}{2},j,kl}, j \le j_0$ (points at Γ_1), only the case $\xi_k < 0$ needs to be defined using complete reflection boundary condition (3.20),

$$
f_{i_0+\frac{1}{2},j,kl} = f_{i_0,j,k_1,l}, \quad \text{with } \xi_{k_1} = -\xi_k.
$$

The numerical fluxes $f_{i,j_0+\frac{1}{2},kl}, i \ge i_0+1$ (points at Γ_2) needs to be defined only in the case $\eta_l > 0$ by the complete reflection boundary condition (3.19)

$$
f_{i,j_0+\frac{1}{2},kl} = f_{i,j_0+1,k,l_1}, \ \text{with } \eta_{l_1} = -\eta_l \, .
$$

All other fluxes are defined by upwind (or its second order TVD extension [29]).

After the spatial discretization is specified, one can use any time discretization for the time derivative.

The diffraction coefficient $D(\theta,\alpha)$ in (3.17) is singular for $r = 0$, which is the vertex of the corner $(x_{i_0+\frac{1}{2}}, y_{j_0+\frac{1}{2}})$. Since in our numerical scheme, we define the numerical flux related to the diffraction at $(x_{i_0+\frac{1}{2}}, y_{j_0+1})$ and $(x_{i_0}, y_{j_0+\frac{1}{2}})$, we simply let $r = \frac{\Delta x}{2}$ in (3.17) to define $D(\theta,\alpha)$ in our computation.

5. Positivity and l^∞ contraction.

Since the exact solution of the Liouville equation is positive when the initial profile is, it is important that the numerical solution inherits this property.

We only consider the scheme using the forward Euler method in time. Without loss of generality, we consider the case $c_{i+\frac{1}{2},j} > c_{i-\frac{1}{2},j}, c_{i,j+\frac{1}{2}} > c_{i,j-\frac{1}{2}}$ for all i,j (the other cases can be treated similarly with the same conclusion). We consider the scheme at (x_{i_0+1}, y_{j_0+1}) (cell III) with $\xi_k < 0, \eta_l > 0$ (the diffraction case. Other

cells can be treated similarly).

$$
\begin{aligned}
&\frac{f^{n+1}_{i_0,j_0+1,kl}-f^{n}_{i_0,j_0+1,kl}}{\Delta t}\\
=&-\frac{c_{i_0,j_0+1}\gamma}{\Delta x}\Big\{\sum_{m=0}^{I}D(\theta_{kl},\alpha_m)f^n_{i_0,j_0}(\xi_{klm},\eta_{klm})\Delta\alpha\\
&+\sum_{m=I+1}^{2I}D(\theta_{kl},\alpha_m)f^n_{i_0,j_0+1}(\xi_{klm},\eta_{klm})\Delta\alpha\\
&+\sum_{m=2I+1}^{3I}D(\theta_{kl},\alpha_m)f^n_{i_0+1,j_0+1}(\xi_{klm},\eta_{klm})\Delta\alpha-f^n_{i_0,j_0+1,kl}\Big\}\\
&-\frac{c_{i_0,j_0+1}\beta}{\Delta y}\Big\{-\sum_{m=0}^{I}D(\theta_{kl},\alpha_m)f^n_{i_0,j_0}(\xi_{klm},\eta_{klm})\Delta\alpha\\
&+\sum_{m=I+1}^{2I}D(\theta_{kl},\alpha_m)f^n_{i_0,j_0+1}(\xi_{klm},\eta_{klm})\Delta\alpha\\
&+\sum_{m=2I+1}^{3I}D(\theta_{kl},\alpha_m)f^n_{i_0+1,j_0+1}(\xi_{klm},\eta_{klm})\Delta\alpha+f^n_{i_0,j_0+1,kl}\Big\}\\
&+R_{kl}C^x_{i_0,j_0+1}\frac{f^n_{i_0,j_0+1,k+1,l}-f^n_{i_0,j_0+1,kl}}{\Delta\xi}\\
&+R_{kl}C^y_{i_0,j_0+1}\frac{f^n_{i_0,j_0+1,k,l+1}-f^n_{i_0,j_0+1,kl}}{\Delta\eta},
\end{aligned}
\tag{5.9}
$$

with $\gamma=\frac{\xi_k}{\sqrt{\xi_k^2+\eta_l^2}}<0$, $\beta=\frac{\eta_l}{\sqrt{\xi_k^2+\eta_l^2}}>0$, $C^y_{i_0,j_0+1}=\frac{c_{i_0,j_0+\frac{3}{2}}-c_{i_0,j_0+\frac{1}{2}}}{\Delta y}$, $C^x_{i_0,j_0+1}=\frac{c_{i_0+\frac{1}{2},j_0+1}-c_{i_0-\frac{1}{2},j_0+1}}{\Delta x}$. The above equation can be rewritten into (we omit the superscript n of f),

$$
\begin{aligned}
&f^{n+1}_{i_0,j_0+1,kl}\\
=&\big(1-c_{i_0,j_0+1}(\lambda_x|\gamma|+\lambda_y|\beta|)-d_1-d_2\big)f_{i_0,j_0+1,kl}+d_1f_{i_0,j_0+1,k+1,l}\\
&+d_2f_{i_0,j_0+1,k,l+1}+c_{i_0,j_0+1}(\lambda_x|\gamma|+\lambda_y|\beta|)\Delta\alpha\Big[\sum_{m=0}^{I}D(\theta_{kl},\alpha_m)f_{i_0,j_0,k_m,l_m}\\
&+\sum_{m=I+1}^{2I}D(\theta_{kl},\alpha_m)f_{i_0,j_0+1,k_m,l_m}+\sum_{m=2I+1}^{3I}D(\theta_{kl},\alpha_m)f_{i_0+1,j_0+1,k_m,l_m}\Big],
\end{aligned}
\tag{5.10}
$$

where $d_1=\frac{|c_{i_0+\frac{1}{2},j_0+1}-c_{i_0-\frac{1}{2},j_0+1}|}{\Delta x}\lambda_\xi R_{kl}$, $d_2=\frac{|c_{i_0,j_0+\frac{3}{2}}-c_{i_0,j_0+\frac{1}{2}}|}{\Delta y}\lambda_\eta R_{kl}$, $\lambda_x=\frac{\Delta x}{\Delta t}$, $\lambda_y=\frac{\Delta y}{\Delta t},\lambda_\xi=\frac{\Delta\xi}{\Delta t}$, $\lambda_\eta=\frac{\Delta\eta}{\Delta t}$.

Now we investigate the positivity of scheme. This is to prove that if $f^n_{ijkl}\ge 0$ for all $(ijkl)$, then this is also true for f^{n+1}. Since the sum of all coefficients in (5.10) is less than 1, one just needs to show that all the coefficients for f^n are non-negative. Because $D(\theta_{kl},\alpha_m)\ge 0$, and $\sum_{m=0}^{3I}D(\theta_{kl},\alpha_m)\le 1$, a sufficient condition for this is clearly

$$1-c_{i,j}(\lambda_x|\gamma|+\lambda_y|\beta|)-d_1-d_2\ge 0$$

or

$$\Delta t \max_{ijkl}\left[\frac{c_{ij}}{\Delta x}+\frac{c_{ij}}{\Delta y}+\frac{\frac{|c_{i+\frac{1}{2},j}-c_{i-\frac{1}{2},j}|}{\Delta x}\sqrt{\xi_k^2+\eta_l^2}}{\Delta\xi}+\frac{\frac{|c_{i,j+\frac{1}{2}}-c_{i,j-\frac{1}{2}}|}{\Delta y}\sqrt{\xi_k^2+\eta_l^2}}{\Delta\eta}\right]\leq 1, \tag{5.11}$$

which means that the scheme is positive when a hyperbolic type CFL condition (5.11) is satisfied.

The l^∞-contracting property of this scheme follows easily, because the coefficients in the schemes are positive and the sum of them is less than 1.

6. **Numerical Examples.** We present numerical examples to demonstrate the validity of our scheme and to show its numerical accuracy in this section. In the numerical computations the second order Runge -Kutta time discretization is used.

Since it is difficult to get the exact solution for this problem, as in [24], we use the numerical solution with the mesh size small enough to represent the exact solution. The two-dimensional Lax-Wendroff method with space mesh size $\Delta x=\Delta y=\frac{\epsilon}{20}$ and $\Delta t=\Delta x/2$ are used to solve the system (2.2) in the form

$$\begin{cases}\dfrac{\partial \mathbf{r}}{\partial t}-\nabla s=0,\\ \dfrac{1}{c(\mathbf{x})^2}\dfrac{\partial s}{\partial t}-\mathrm{div}\mathbf{r}=0,\end{cases}$$

with $s=\frac{\partial u}{\partial t},\mathbf{r}=\nabla u$ to get the energy density distribution

$$\mathcal{E}(\mathbf{x},t)=\frac{1}{2}\frac{1}{c(\mathbf{x})^2}|s|^2+\frac{1}{2}|\mathbf{r}|^2. \tag{6.12}$$

The numerical energy density is defined as

$$\mathcal{E}_{ij}=\frac{1}{2}\frac{1}{c_{ij}^2}|s_{ij}|^2+\frac{1}{2}|\mathbf{r}_{ij}|^2, \tag{6.13}$$

where

$$s_{ij}=\frac{1}{\Delta x\Delta y}\int_{x_{i-1/2}}^{x_{i+1/2}}\int_{y_{i-1/2}}^{y_{i+1/2}}s(x,y)dxdy,$$

and $\mathbf{r}_{ij}$ can be defined similarly.

The discrete wave equation is quite dispersive [7], so one needs many grid points per wavelength to compute it. The mesh size $h=\epsilon/20$ is the biggest mesh size we can get satisfactory numerical results for the discrete wave equation.

The limit energy density is the zeroth moment of the density distribution of Liouville equation

$$\mathcal{E}^{(0)}(x,y,t)=\int\int f(x,y,\xi,\eta,t)d\eta d\xi.$$

The computational tool we used is the super computer in Tsinghua National Laboratory for Information Science and Technology, 512 Itanium 2 64 bit processor. The peak computational speed is of 2.662×10^{13}, the total EMS memory is 1024G, and the storage space is 26T.

In the computation, we first approximate the delta function initial data of the Liouville equation by the product of a discrete delta function in 1-D [12]:

$$\delta_\omega(x) = \begin{cases} \frac{1}{\omega}(1 - |\frac{x}{\omega}|), & |\frac{x}{\omega}| \le 1, \\ 0, & |\frac{x}{\omega}| > 1, \end{cases} \tag{6.14}$$

with $\omega = \Delta\xi = \Delta\eta$. (For more recent numerical studies on the approximations of the delta function, see [36, 38, 39, 40, 41]). Then the energy density distribution are recovered by

$$\mathcal{E}_{ij}^{(0)} = \sum_{kl} f_{ijkl}\Delta\xi\Delta\eta. \tag{6.15}$$

We use the L^1-error in the cumulative distribution function (cdf), i.e., the anti-derivative of energy density [15]

$$\int_{-\infty}^{+\infty}\int_{-\infty}^{+\infty}\Big|\int_{-\infty}^{x}\int_{-\infty}^{y}\mathcal{E}^{(0)}(s,z,t) - \mathcal{E}(s,z,t)dsdz\Big|dxdy, \tag{6.16}$$

which can be expected to flatten as ϵ is decreased, to measure the weak convergence in the semiclassical limit. Lemma 2.1 in [3] ensures that (6.16) going to zero is equivalent to the weak convergence of $\mathcal{E}^{(0)}(x,y,t)$

For a more through discussion about the model error and numerical discretization error of this approach we refer to our previous work [24].

Example 6.1. Consider the wave equation on the domain with boundary $\Gamma_1 = \{(x,y)|\ x \ge 0.2, y = 0.3\}$ and $\Gamma_2 = \{(x,y)|\ x = 0.2, y \le 0.3\}$.

$$\begin{cases} \dfrac{\partial^2 u}{\partial t^2} - c(x,y)^2\Delta u = 0, \\ u(0) = 4\epsilon e^{i\frac{(x^2+y^2)}{5\epsilon} - 100x^2 - 100y^2}, \\ \dfrac{\partial u}{\partial t}(0) = 0, \end{cases} \tag{6.17}$$

where $\epsilon = 1/2000, c(x,y) = 2$ and suitable boundary conditions must be given on Γ_1 and Γ_2.

The corresponding Liouville equation is

$$f_t + \frac{2\xi}{\sqrt{\xi^2+\eta^2}}f_x + \frac{2\eta}{\sqrt{\xi^2+\eta^2}}f_y = 0, \tag{6.18}$$

with initial data

$$f(0,\mathbf{x},\mathbf{v}) = 4(x^2+y^2)e^{-200(x^2+y^2)}\delta\Big(\xi - 0.4x\Big)\delta\Big(\eta - 0.4y\Big).$$

The computation domain is $[x,y,\xi,\eta] \in [-1,1]\times[-1,1]\times[-1,1]\times[-1,1]$, and time step is $\Delta t = \frac{1}{3}\Delta x$.

Firstly, we consider the problem with the soft boundary condition on Γ_i, i.e. $u\big|_\Gamma = 0, i = 1,2$. The physically relevant values for the diffraction coefficient $D^-(\theta,\alpha)$ are given by (3.17).

For convenience, we denote our scheme by GTD, and the scheme for Liouville equation with complete reflection boundary condition (Geometric optics) by GO. Figure 4 shows the numerical energy densities $\mathcal{E}$, GTD and GO at $t = 0.2, 0.3$. One can see that there are some diffracted waves behind the corner-the shadow zone. The numerical results of GTD can capture the average energy of the solution of the

wave equation, including the shadow zone, which is below the line connecting the corner and point $(1, 1)$.

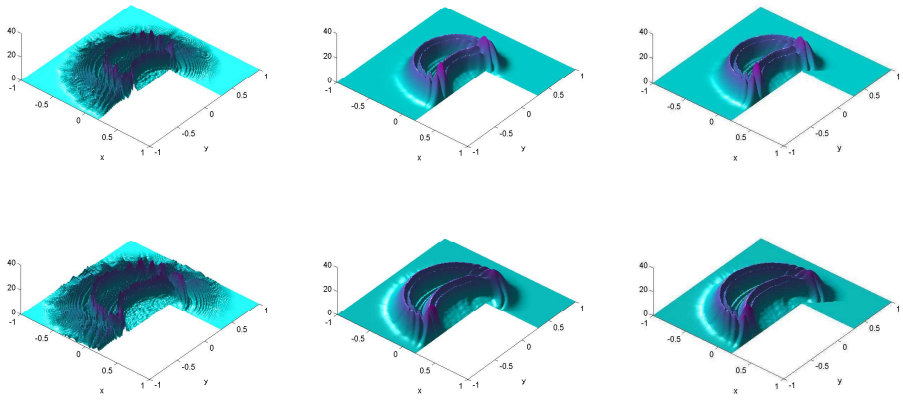

FIGURE 4. Energy density with soft boundary at $t = 0.2$ (top) and $t = 0.3$ (bottom). left: $\mathcal{E}$, middle: GTD, right GO .

Table 1 gives the l^1-errors of numerical GTD (defined in (6.16) but numerically evaluated by the Riemann sum over all cells) at $t = 0.1, 0.2$ and 0.3 on different meshes. The convergence rate is about 1.

TABLE 1. errors of GTD with soft boundary

mesh type	$50^2 \times 50^2$	$100^2 \times 100^2$	$200^2 \times 200^2$	$400^2 \times 400^2$
t=0.1	3.3604e-2	1.6302e-2	7.9748e-3	3.9505e-3
t=0.2	3.7204e-2	1.8449e-2	9.1946e-3	4.5508e-3
t=0.3	4.1802e-2	2.0843e-2	9.9872e-3	4.9725e-3

Table 2 shows the errors of the numerical energy density GTD in the shadow zone ($x \geq 0.2, y \leq x + 0.1$). The GTD solution is a good approximation to the solution of the wave equation in the shadow zone. Notice that the convergence rate in the shadow region is smaller than first order. This is partly because that there is a boundary layer near the shadow boundary, which is harder to resolve numerically then elsewhere.

The solutions of GTD and GO depend on wavelength ϵ. Fig. 5 gives, at $t = 0.2$, the relation between the error of GTD and GO and the wavelength ϵ. One can see that the error of solution of GO and GTD is of same order–near $O(\epsilon)$, which is consistent with the theoretic analysis.

Next, we consider the problem with the hard boundary condition on $\Gamma_i, i = 1, 2$, i.e. $\frac{\partial u}{\partial n}\big|_{\Gamma_i} = 0, i = 1, 2$. We use the extrapolation boundary condition for the Lax-Wendroff method in the fully resolved simulation of the high frequency wave

TABLE 2. error of energy density GTD with soft boundary in shadow region

mesh type	$50^2 \times 50^2$	$100^2 \times 100^2$	$200^2 \times 200^2$	$400^2 \times 400^2$
t=0.1	10%	5.1%	4.6%	4.3%
t=0.2	12%	5.9%	5.0%	4.6%
t=0.3	14%	6.9 %	5.5%	5.1%

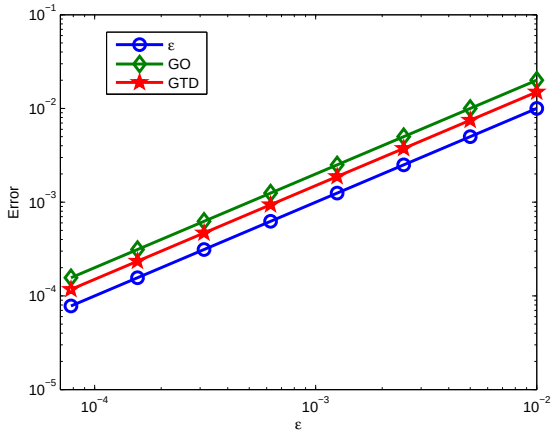

FIGURE 5. The relation between errors of GO and GTD and ϵ

equation. The physically relevant values for the diffraction coefficient $D^+(\theta, \alpha)$ are given by (3.17).

Figure 6 shows the numerical energy densities $\mathcal{E}$, GTD, and GO, at $t = 0.2, 0.3$. One can see that the energy of the diffracted waves behind the corner-the shadow zone is stronger than the case of the soft boundary condition. The numerical results of GTD is very close to the solution of the wave equation. Table 3 presents errors of the numerical energy density by GTD computed with different meshes in the phase space at $t = 0.1, 0.2$ and 0.3. The convergence rate is of first order.

TABLE 3. Errors of GTD of Example 5.1 with the hard boundary

mesh type	$50^2 \times 50^2$	$100^2 \times 100^2$	$200^2 \times 200^2$	$400^2 \times 400^2$
t=0.1	2.8456e-2	1.4209e-2	7.1033e-3	3.5606e-3
t=0.2	3.2144e-2	1.5965e-2	7.8306e-3	3.8948e-3
t=0.3	3.8442e-2	1.9204e-2	9.1002e-3	4.5453e-3

Table 4 shows the errors of the numerical energy density GTD in the shadow zone. The GTD solution is a good approximation to the solution of the wave equation in the shadow zone.

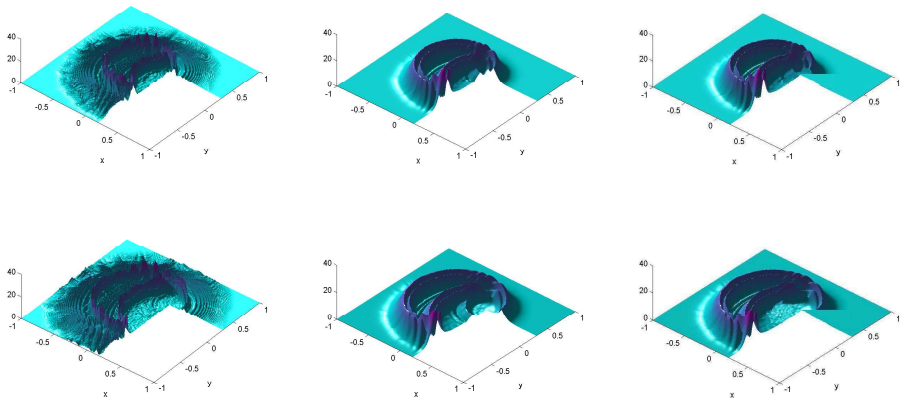

FIGURE 6. Energy density with hard boundary at $t = 0.2$ (top) and $t = 0.3$ (bottom). left: $\mathcal{E}$, middle: GTD, right GO.

TABLE 4. Errors of GTD for Example 5.1 with hard boundary in the shadow zones

mesh type	$50^2 \times 50^2$	$100^2 \times 100^2$	$200^2 \times 200^2$	$400^2 \times 400^2$
t=0.1	11.2%	6.0%	4.7%	4.1%
t=0.2	13.6%	7.6%	5.2%	4.6%
t=0.3	17.8 %	10.7 %	5.8%	5.2%

Example 6.2. Consider the wave equation in 2D with a rectangle boundary Ω:

$$\begin{cases} \dfrac{\partial^2 u}{\partial t^2} - c(x,y)^2 \Delta u = 0, \\ u(0) = 8\epsilon e^{i\frac{(x^2+y^2)}{5\epsilon} - 50x^2 - 50y^2}, \\ \dfrac{\partial u}{\partial t}(0) = 8 e^{i\frac{(x^2+y^2)}{5\epsilon} - 50x^2 - 50y^2}, \end{cases} \tag{6.19}$$

with $\epsilon = 1/4000$, $c(x,y) = 2(1-x)^2$, $\Omega = \big\{(x,y) \,|-0.3 \le x \le 0.1, -0.5 \le y \le -0.2\big\}$ and some suitable boundary conditions on Ω.

The corresponding Liouville equation is

$$f_t + \frac{c(x,y)\xi}{\sqrt{\xi^2+\eta^2}} f_x + \frac{c(x,y)\eta}{\sqrt{\xi^2+\eta^2}} f_y - c_x\sqrt{\xi^2+\eta^2} f_\xi - c_y\sqrt{\xi^2+\eta^2} f_\eta = 0, \tag{6.20}$$

with initial data

$$f(0,\mathbf{x},\mathbf{v}) = 32\left[0.16(x+y)^2 + \frac{1}{c(x,y)^2}\right] e^{-400x^2-400y^2} \delta\Big(\xi - 0.4x\Big)\delta\Big(\eta - 0.4y\Big).$$

The computational domain is chosen to be $[x,y,\xi,\eta] \in [-1,1]\times[-1,1]\times[-1,1]\times[-1,1]$. The time step is chosen as $\Delta t = \frac{1}{4}\Delta x$.

Firstly, we simulate the problem with the soft boundary condition. The physically relevant values for the diffraction coefficient $D^-(\theta,\alpha)$ is given by (3.17).

Figure 7 shows the numerical energy densities $\mathcal{E}$, GTD and GO at $t = 0.2, 0.3$. The numerical results of GTD is very close to the solution of the wave equation, even in the shadow zone.

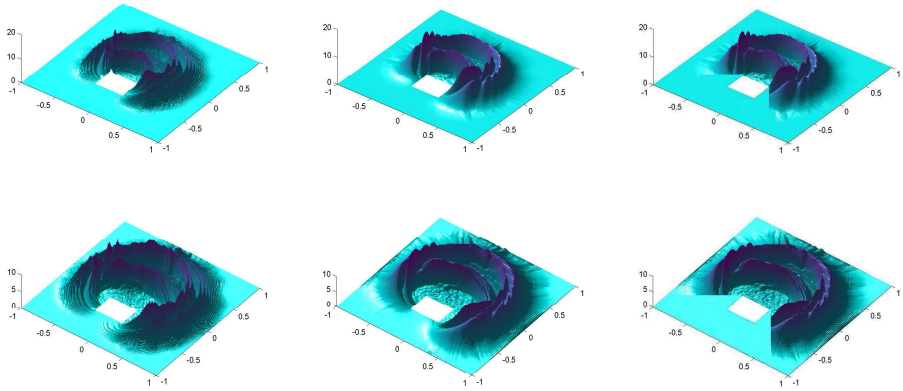

FIGURE 7. Energy density with soft boundary at $t = 0.2$ (top) and $t = 0.3$ (bottom). left: $\mathcal{E}$, middle: GTD, right GO.

Table 5 presents the errors of the numerical energy density GTD computed with different meshes in the phase space at $t = 0.1, 0.2$ and 0.3. The error is very small. The convergence rate is about first order.

TABLE 5. Errors of numerical density GTD of Example 5.2 with the soft boundary

mesh type	$50^2 \times 50^2$	$100^2 \times 100^2$	$200^2 \times 200^2$	$400^2 \times 400^2$
t=0.1	2.4043e-2	1.2021e-2	6.0010e-3	3.0006e-3
t=0.2	2.7024e-2	1.3512e-2	6.7442e-3	3.3721e-3
t=0.3	3.1498e-2	1.5248e-2	7.6118e-3	3.8047e-3

Table 6 shows the errors of the numerical energy density GTD in the shadow zone. The GTD solution is a good approximation to the solution wave equation in the shadow zone ($y < -0.5$).

Finally, we consider the problem with the hard boundary condition on Ω. The physically relevant values for the diffraction coefficient $D^+(\theta,\alpha)$ are given by (3.17).

Table 7 presents the errors of the numerical energy density GTD computed with different meshes in the phase space at $t = 0.1, 0.2$ and 0.3. The convergence rate is about first order.

TABLE 6. Errors of GTD for Example 5.2 with the soft boundary in the shadow zones

mesh type	$50^2 \times 50^2$	$100^2 \times 100^2$	$200^2 \times 200^2$	$400^2 \times 400^2$
t=0.1	10.2%	6.4%	5.1%	4.4%
t=0.2	13.1%	7.0%	5.5%	5.0%
t=0.3	15.7%	9.4 %	6.1%	5.5%

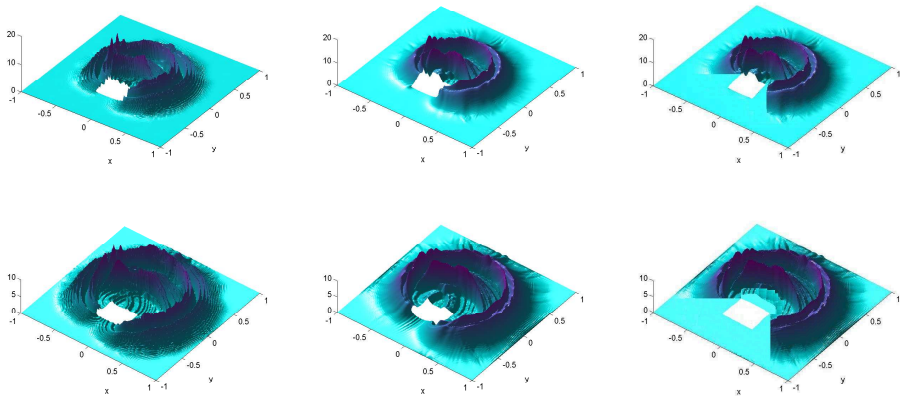

FIGURE 8. Energy density with soft boundary at $t = 0.1$ (top) and $t = 0.2$ (bottom). left: $\mathcal{E}$, middle: GTD, right GO.

TABLE 7. Errors of numerical density GTD of Example 5.2 with the hard boundary

mesh type	$50^2 \times 50^2$	$100^2 \times 100^2$	$200^2 \times 200^2$	$400^2 \times 400^2$
t=0.1	2.4642e-2	1.2176e-2	6.0538e-3	3.0264e-3
t=0.2	2.6054e-2	1.3027e-2	6.5013e-3	3.2489e-3
t=0.3	2.8985e-2	1.4464e-2	7.2192e-3	3.6092e-3

Table 8 shows the errors of the numerical energy density GTD in the shadow zone. The GTD solution is a good approximation to the solution of wave equation in the shadow zones.

Remark 1. The typical wave length of visible lights is $400 - 700$ nanometers, or in the order of 10^{-6} meters. To simulate such a high frequency wave in a domain of one meter requires at least $O(10^6)$ mesh points per spatial dimension. It means $O(10^6)$ meshes in one space dimension, $O(10^{12})$ meshes in two space dimension and $O(10^{18})$ meshes in three dimension. By including the time direction, one needs

TABLE 8. relative l^1 error of GTD for Example 5.2 with the hard boundary in the shadow zones

mesh type	$50^2 \times 50^2$	$100^2 \times 100^2$	$200^2 \times 200^2$	$400^2 \times 400^2$
t=0.1	10.1%	6.3%	4.7%	4.2%
t=0.2	13.6%	6.5%	5.1%	4.6%
t=0.3	16.4%	9.6 %	5.5%	5.0%

$O(10^{18})$ operations in two space dimension and $O(10^{24})$ in three space dimension. This is simply impossible for today's computational equipments.

On the other hand, by using the Liouville equation, although the dimension is doubled, even to resolve the diffraction the mesh size of $O(\epsilon^{1/2}) = O(10^{-3})$, one needs $O(10^{12})$ meshes in two space dimension and $O(10^{18})$ meshes in three space dimension (six dimension in the phase space). But in the time direction, the mesh size is of $O(\epsilon^{1/2})$. So including the time direction, one needs $O(10^{15})$ operations in two space dimension and $O(10^{21})$ in three space dimension. This is about 1000 times less operations compared to the full simulation based on the original wave equation. Thus double the dimension using the Liouville equation provides a much more efficient approach to high frequency waves when the frequency is very high.

It is important also to point out that only near the vertex we need to impose $\Delta x, \Delta y \sim O(\epsilon^{1/2})$. Away from it we can use $\Delta x, \Delta y, \Delta\xi, \Delta\eta = O(1)$ if we program the method in the adaptive mesh framework. This will be a tremendous saving compared with the full wave simulation.

7. **Conclusion.** In this paper, we revise our previous work [25] to a different geometry, namely, high frequency waves through a corner. When a wave hits a corner, it usually reflects. However, at the vertex of the corner, it generates diffracted waves into *all* directions. In particular, the diffracted waves can reach the shadow zone–the zone that the GO theory cannot cover. We provide a diffraction condition, based on the GTD theory, at the vertex to reflect this diffraction nature. We then build this condition, as well as the reflection boundary condition, into the numerical flux of the Liouville solver, in order to capture the diffractions. This gives an Eulerian computational method for high frequency waves through a corner, which is able to capture wave reflection and diffractions at a corner without fully resolving the high frequency waves in the entire computational domain.

The initial data were chosen to be the WKB form (1.2)-(1.3). For more general initial data one could use an initial data decomposition, for example a Gaussian beam type [37], so they become a linear superposition of initial data of this form. Each of the decomposed solutions can be constructed by the approach of this paper. Due to the linearity of the problem one just needs to superimpose the decomposed solutions.

This paper deals with only the right corner. For corners of different angle γ, the same approach can still apply, but one must use a geometry-aligned mesh for the implementation of this approach.

The Liouville or geometrical optics based approach is very effective for very small ϵ. For moderate ϵ one could use other more accurate approaches, one example being

the Gaussian beam method which can also be cast in the Eulerian framework using Liouville equations [23].

Similar ideas, including those in our previous work [25], can also be applied to other geometries, and to elastic and electromagnetic waves, which will be the subjects of future research.

Acknowledgments. The authors would like to thank Tsinghua National Laboratory for Information Science and Technology, China, for computing support. We thank the IPAM at UCLA for its stimulating research environment and warm hospitality.

REFERENCES

[1] J.-D. Benamou, *An introduction to Eulerian geometrical optics(1992-2002)*, J. Sci. Comp., **19** (2001), 63–93.
[2] A. K. Bhattacharyya, "High-Frequency Electromagnetic Techniques: Recent Advances and Application," John Wiley & Sons, Inc., 1995.
[3] Y. Brenier and E. Grenier, *Strickly particles and scalar conservation laws*, SIAM, J. Num. Anal., **38** (1998), 2317–2328.
[4] R. N. Buchal and J. B. Keller, *Boundary layer problems in diffraction theory*, Comm. Pure Appl. Math., **13** (1960), 85–114.
[5] V. Cěrvený, "Seismic Ray Theory," Cambridge University Press, 2001.
[6] L.-T. Cheng, H.-L. Liu and S. Osher, *Computational high-frequency wave propagation using the Level Set method, with applications to the semi-classical limit of Schrödinger equations*, Comm. Math. Sci., **1** (2003), 593–621.
[7] G. Cohen, "Higher-Order Numerical Methods for Transient Wave Equations," Springer, Berlin; New York, 2002.
[8] M. G. Crandall and P.-L. Lions, *Viscosity solutions of Hamilton-Jacobi equations*, Trans. Amer. Math. Soc., **277** (1983), 1–42.
[9] G. A. Deschamps, *High frequency diffraction by wedges*, IEEE Transactions on Antennas and Propagation. AP-**33** (1985), 357–368.
[10] B. Engquist and O. Runborg, *Computational high frequency wave propagation*, Acta Numerica, **12** (2003), 181–266.
[11] B. Engquist, O. Runborg, and A.-K. Tornberg, *High frequency wave propagation by the segment projection method*, J. Comput. Phys., **178** (2002), 373–390.
[12] B. Engquist, A. -K. Tornberg and R. Tsai, *Discretization of dirac delta functions in level set methods*, J. Comput. Phys., **207** (2005), 28–51.
[13] E. Fatemi, B. Engquist and S. Osher, *Numerical solution of the high frequency asymptotic expansion for the scalar wave equation*, J. Comput. Phys., **120** (1995), 145–155.
[14] S. Fomel and J. A. Sethian, *Fast phase space computation of multiple arrivals*, Proc. Natl. Acad. Sci. USA, **99** (2002), 7329–7334.
[15] L. Gosse and N. J. Mauser, *Multiphase semicalssical approximation of an electron in a one-dimensional crystalline lattice – III. From ab initio models to WKB for Schrödinger-Poisson*, J. Comput. Phys., **211** (2006), 326–346.
[16] S. Jin and X. Li, *Multi-phase computations of the semiclassical limit of the Schrödinger equation and related problems: Whitham vs Wigner*, Physics D, **182** (2003), 46–85.
[17] S. Jin and X. Liao, *A Hamiltonian-preserving scheme for high frequency elastic waves in heterogeneous media*, J. Hyperbolic Diff Eqn., **3** (2006), 741–777.
[18] S. Jin, H. L. Liu, S. Osher and R. Tsai, *Computing multi-valued physical observables for high frequency limit of symmetric hyperbolic systems*, J. Comp. Phys., **210** (2005), 497–518.
[19] S. Jin and S. Osher, *A level set method for the computation of multi-valued solutions to quasi-linear hyperbolic PDEs and Hamilton-Jacobi equations*, Comm. Math. Sci., **1** (2003), 575–591.
[20] S. Jin and X. Wen, *Hamiltonian-preserving scheme for the Liouville equation with discontinuous potentials*, Comm. Math. Sci., **3** (2005), 285–315.
[21] S. Jin and X. Wen, *A Hamiltonian-preserving scheme for the Liouville equation of geometric optics with partial transmissions and reflections*, SIAM J. Num. Anal., **44** (2006), 1801–1828.

[22] S. Jin and X. Wen, *Computation of transmissions and reflections in geometric optics via the reduced Liouville equation*, Wave Motion, **43** (2006), 667–688.
[23] S. Jin, H. Wu and X. Yang, *Gaussian beam methods for the Schrodinger equation in the semi-classical regime: Lagrangian and Eulerian formulations*, Comm. Math. Sci., **6** (2008), 995–1020.
[24] S. Jin and D. S. Yin, *Computational high frequency waves through curved interfaces via the Liouville equation and geometric theory of diffraction*, J. Comput. Phys., **227** (2008), 6106–6139.
[25] S. Jin and D. S. Yin, *Computation of high frequency wave diffraction by a half plane via the Liouville equation and geometric theory of diffraction*, Communications in Computational Physics, **4** (2008), 1106–1128.
[26] J. B. Keller, *Geometric theory of diffraction*, J. Opt. Soc. of America, **52** (1962), 116–130.
[27] J. B. Keller and R. Lewis, *Asymptotic methods for partial differential equations: The reduced wave equation and maxwell's equations*, In "Surveys in Applied Mathematics"(eds. D. McLaughlin J. B. Keller and G. Papanicolaou), Plenum Press, New York, 1995.
[28] R. G. Kouyoumjian and P. H. Parthak, *A uniform geometrical theory of diffraction for an edge in a perfectly conducting surface*, Proc. Of the IEEE, **62** (1974), 1448–1461.
[29] R. LeVeque, "Numerical Methods for Conservation Laws," Birkhauser, 1992.
[30] L. Miller, *Refraction of high-frequency waves density by sharp interfaces and semiclassical measures at the boundary*, J. Math. Pures Appl., **79** (2000), 227–269.
[31] M. Motamed and O. Runborg, *A fast phase space method for computing creeping rays*, J. Comput. Phys., **219** (2006), 276–295.
[32] M. Motamed and O. Runborg, *A multiple-patch phase space method for computing trajectories on manifolds with applications to wave propagation problems*, Commun. Math. Sci., **5** (2007), 617–648.
[33] S. Osher, L. T. Cheng, M. Kang, H. Shim and Y. -H. Tsai, *Geometric optics in a phase-space-based level set and Eulerian framework*, J. Comput. Phys., **179** (2002), 622–648.
[34] L. Ryzhik, G. Papanicolaou and J. Keller, *Transport equations for elastic and other waves in random media*, Wave Motion, **24** (1996), 327–370.
[35] C. Sparber, N. Mauser and P. A. Markowich, *Wigner functions vs. WKB techniques in multivalued geometric optics*, J. Asympt. Anal., **33** (2003), 153–187.
[36] P. Smereka, *The numerical approximation of a delta function with application to level set methods*, J. Comput. Phys., **211** (2006), 77–90.
[37] N. M. Tanushev, B. Engquist and R. Tsai, *Gaussian beam decomposition of high frequency wave fields*, J. Comp. Phys., **228** (2009), 8856–8871.
[38] J. D. Towers, *Two methods for discretizing a delta function supported on a level set*, J. Comput. Phys., **220** (2007), 915–931.
[39] X. Wen, *High order numerical methods to a type of delta function integrals*, J. Comput. Phys., **226** (2007), 1952–1967.
[40] X. Wen, *High order numerical methods to two dimensional delta function integrals in level set methods*, J. Comput. Phys., **228** (2009), 4273–4290.
[41] X. Wen, *High order numerical methods to three dimensional delta function integrals in level set methods*, SIAM J. Sci. Comput., **32** (2010), 1288–1309.
[42] L. Ying and E. J. Candés, *Fast geodesics computation with the phase flow method*, J. Comput. Phys., **220** (2006), 6–18.

Received August 2010; revised November 2010.

E-mail address: jin@math.wisc.edu
E-mail address: dyin@math.tsinghua.edu.cn